Study of limit strains for FCC and BCC sheet metal using polycrystal plasticity

M.J. Serenelli, M.A. Bertinetti, J.W. Signorelli *

Instituto de Física Rosario (IFIR), CONICET – UNR, 27 de febrero 210 bis (2000) Rosario, Argentina

ARTICLE INFO

ABSTRACT

In this research, we analyze forming-limit strains of FCC and BCC materials using a viscoplastic self-consistent polycrystal model (VPSC) in conjunction with the Marciniak–Kuczynski (MK) approach. In particular, our work is focused on the theoretical analysis and comparison between FCC and BCC crystal structures made by Inal et al. [Inal, K., Neale, K.W., Aboutajeddine, A., 2005. Forming limit comparison for FCC and BCC sheets, International Journal of Plasticity, 21, 1255–1266]. These authors performed their simulations based on a generalized Taylor-type polycrystal model (MK-FC), finding a remarkably low forming-limit curve for the FCC material and an extremely high forming-limit curve for the BCC material, in the biaxial stretching range. We verified that our predictions are similar to Inal's results for both FCC and BCC materials when the MK-FC model is used. However, MK-VPSC calculations do not give such extreme values, and we believe that this theory predicts much more reliable results for both FCC and BCC crystallographic assumptions. We also found that localized necking depends on texture evolution in the vicinity of equi-biaxial stretching, through the sharpness of the predicted yield surface. Finally, it is shown that the MK-VPSC's predictions are in good agreement with experimental data for AA5182-O and a DQ-type steel-sheet metal.

1. Introduction

Formability of sheet metals can be characterized by the forming limit diagram (FLD) introduced by Keeler and Backofen, 1964. This concept has proved useful for representing conditions at the onset of sheet necking and now is a standard tool for characterizing the material forming behavior. The FLD represents, in one map, all combinations of critical-limit surface strains corresponding to failure. Within the FLD, a line called the forming-limit curve (FLC) marks the onset of local necking and divides strain space into safe and failure zones. The object of sheet-metal process design is to ensure that strains in the sheet do not approach this limit curve. Though the concept of the FLD is simple, a material's ability to deform plastically depends on a large number of coupled effects, making its experimental determination non trivial and a very time consuming procedure. As a result, considerable effort has recently been made to develop theoretical predictive models, based on the continuum theory of plasticity and different instability criteria. Among these, models enjoying particular success are those where the strain instability appears in the deformation process due to an imperfection already present in the material. In particular, Marciniak and Kuczynski (1967), developed probably the most influential approach for initiating localized necking. According to this model, an infinite sheet contains a local imperfection region, which is a band having an initial thickness less than that of the sheet. These authors showed that the presence of such an imperfection can lead to unstable deformation in the thinner region and subsequent localized necking and failure.

As Wu et al. (2005) pointed out, within the M–K framework, the influence of various constitutive features on FLDs has been explored using phenomenological plasticity models and crystal plasticity. Authors have tested the implementation of different yield criteria in the M–K model. In particular, Cao et al. (2000) predicted localized thinning of sheet metal alloys combining the M–K analysis with a general anisotropic yield criterion. Banabic and Dannenmann (2001) used the yield criterion proposed by Hill, 1993 for calculations of the limit strains in connection with Swift's instability condition for diffuse necking. Using the M–K theory, Butuc et al. (2002) investigated the performance of two non quadratic yield functions applicable to orthotropic sheet metals, Yld96 and BBC2000, for making forming-limit predictions. Later, Butuc et al. (2003) conducted necking simulations based on a M–K defect using the Yld96 yield function and a combined model of texture and strain-path induced anisotropy. They found that, for a BH steel sheet when the strain path is complex, the microstructural hardening model with a texture-based yield locus is superior to the phenomenological approaches. However, they did not take texture evolution into account. Ávila and Vieira (2003) proposed an algorithm for the prediction of the right side of the FLD using the methodology proposed by Marciniak and Kuczynski, with five different yield criteria. They concluded that the type of yield criteria used in

* Corresponding author. Tel./fax: +54 341 480 8545.
  E-mail address: signorelli@ifir-conicet.gov.ar (J.W. Signorelli).

the analysis strongly influences the FLD. Banabic et al. (2004) included the BBC2000 yield criterion in the classical M–K approach, and compared their predictions with experimental data for an aluminium alloy. In a manner similar to the later investigation of Butuc et al. (2003); Hiwatashi et al. (1998) developed a model which can describe mechanical behaviors on the basis of texture and dislocation structure. They applied their model in conjunction with the M–K approach to predict FLDs, finding that their calculations successfully predicted some of the experimental tendencies, which cannot be reproduced by conventional phenomenological models. This suggests that the latent hardening contribution reduces the forming-limit strains for particular strain-path changes.

It is well known that texture evolution, and hence anisotropy, strongly affects FLDs, and the previous approaches do not address this important point. Though analytical yield-criteria analyses are able to describe the effects of initial anisotropy, they still have difficulty accounting for the evolution of yield surfaces. These effects can be taken into account naturally by using polycrystal plasticity models. Issues such as yield-surface shape, changes of sharpness, material anisotropy and crystal orientation are directly addressed within a polycrystalline model. Zhou and Neale (1995) used a viscoplastic, polycrystalline model based on a full-constraint (FC) transition scale in the M–K analysis to predict FLDs for annealed FCC material. Wu et al. (1997, 1998), using a rate-sensitive polycrystal model in conjunction with the same M–K approach, performed numerical simulations of FLDs of rolled aluminum sheets. With this formulation, they assessed the effects of crystal plasticity, strain-rate sensitivity and hardening. Knockaert et al. (2002) developed a rate-independent Taylor polycrystal model to calculate limit strains in AA6116-T4. Such material modeling takes the evolution of the crystallographic texture during forming into account, and further improves the accuracy of FLC predictions. Later, Wu et al. (2004a) and Yoshida et al. (2007) analyzed the effect of the cube texture and other typical rolling-texture components on forming-limit strains. Wu et al. (2007) studied the effects of spatial orientation distribution, material strain-rate sensitivity, texture evolution and initial surface topography on sheet-metal necking. They numerically simulated localized necking in AA6111-T4 under stretching, and electron backscatter diffraction (EBSD) texture measurement results for the sheet were directly incorporated into a crystal-plasticity based finite-element code. In their work, they assumed that localized necking was associated with surface instability, and that the artificial initial imperfection required by the M–K approach was not relevant. They found that localized necking depends on both the initial texture and its spatial orientation distribution. Recently, Signorelli et al. (2009) incorporated the viscoplastic (VP) self-consistent (SC) scheme within the M–K methodology (MK-VPSC), and performed a detailed parametric study – analyzing the effects of initial imperfection, rate-sensitivity and hardening – to validate their approach. They found that the incorporation of the crystallographic texture-induced anisotropy and its evolution may lead to a better prediction of the AA5182-O FLD. Neil and Agnew (2009) used the same framework, considering dislocation-based plasticity as well as mechanical twinning in order to treated magnesium alloys. They showed that the initial texture has a strong influence upon formability, and more random initial textures would be a promising area for Mg alloy/process development. This hypothesis was recently confirmed by Dreyer et al. (2010).

Materials with different crystallographic structures will have different forming-limit curves. In general, investigators have observed lower limit-strain values in the right-hand side (RHS) of the FLD for aluminum alloys than for steel sheets. These results verify that FCC materials have a worse formability than BCC materials (Barlat, 1987; Butuc, 2004). In the former case, low limit strains are reported by many authors using MK-FC approach –

see e.g. Zhou and Neale (1995), Wu et al. (2004a), Viatkina et al. (2005), Yoshida et al. (2007) – for the RHS, especially close to the equi-biaxial zone. These results are a characteristic of the FC model when the initial texture has a very low intensity or a random distribution (Signorelli et al., 2009; Signorelli and Bertinetti, 2009). On the other hand, the measured forming-limit curves for the BCC assumption do not show the high values achieved when calculations are carried out with the MK-FC approach (Hiwatashi et al. (1998), Inal et al. (2005)). Particularly, the effect of different BCC slip assumptions was recently discussed by the authors (Serenelli et al., 2010); we found that the number of available crystallographic slip systems and the type of crystal plasticity model strongly affects the calculated limit strains on the RHS of the FLD.

In the present study, the effects of the polycrystalline model on the FLD predictions are evaluated, focusing on the analysis of the FCC-BCC comparison introduced by Inal et al. (2005). These authors performed numerical simulations using 12 and 24 slip systems for FCC and BCC materials, respectively. They reported a remarkably low forming-limit curve for the FCC material and an extremely high forming-limit curve for the BCC one. In what follows, we will show that the calculations carried out with the MK-VPSC model provide more realistic results than those obtained from the MK-FC approach. MK-VPSC calculations do not show those extreme values, predicting much more reliable values for both FCC and BCC materials. We also found that localized necking depends on texture evolution in the vicinity of equi-biaxial stretching, through the sharpness of the predicted yield surface, which is consistent with the work of Neale and Chater (1980) and Lian et al. (1989). Our present paper specifically aims to highlight that the assumed homogenization scheme plays an important role, which cannot be omitted in the discussion of the simulation's results. The predicative capability of a particular plasticity model is then assessed by comparing its predictions with those experimental data not used for the fitting. In our case, the discussion is framed in terms of the predicted FLD, texture evolution and polycrystal yield surface.

We begin Section 2 with a review of the basic equations and definitions for the M–K and VPSC theories. In Section 3, the predicted FLDs for both FCC and BCC materials are evaluated. Comparison with the MK-FC approach is also included. Details of the advantages of using VPSC as the material model in the M–K are discussed. In Section 4 the MK-VPSC predictions are compared with experimental data for AA6116-T4 and DQ-type (drawing quality) steel sheet metal. Finally, we summarize results and state conclusions in Section 5.

2. Theoretical framework

2.1. Viscoplastic crystal plasticity

For simplicity we will restrict the present discussion to a viscoplastic formulation. For metals, this is a common assumption in large-strain plasticity, where the elastic components are at least two orders of magnitude less than the plastic contributions. Using a dot to indicate time derivate, the velocity gradient tensor is:

$$\mathbf{L} = \dot{\mathbf{F}} : \mathbf{F}^{-1} = \dot{\mathbf{R}}^* : \mathbf{R}^{*^\mathrm{T}} + \mathbf{R}^* : \mathbf{L}^\mathrm{p} : \mathbf{R}^{*^\mathrm{T}}. \tag{1}$$

In this expression, $\mathbf{R}^*$ represents the crystallographic rotation, $\mathbf{F}$ corresponds to the effect of dislocation slip on crystal deformation, and $\mathbf{L}^\mathrm{p} = \dot{\mathbf{F}}^\mathrm{p} : \mathbf{F}^{\mathrm{p}^{-1}}$ is the plastic velocity gradient that results from dislocation motion along specific planes and directions of the crystal (all potentially activated slip systems are labeled with the superscript s):

$$\mathbf{L}^\mathrm{p} = \sum_s \left(\mathbf{n}^s \otimes \mathbf{b}^s \right) \dot{\gamma}^s, \tag{2}$$

$\dot{\gamma}^s$ represents the dislocation slip rates, $\mathbf{n}^s$ and $\mathbf{b}^s$ are the normal to the system's or systems' glide plane and the Burgers vector, respectively. They define the symmetric and the screw-symmetric parts of the Schmid orientation tensor:

$$\mathbf{m}^s = \frac{1}{2}\left(\mathbf{n}^s \otimes \mathbf{b}^s + \mathbf{n}^s \otimes \mathbf{b}^s\right), \tag{3}$$

$$\mathbf{q}^s = \frac{1}{2}\left(\mathbf{n}^s \otimes \mathbf{b}^s - \mathbf{n}^s \otimes \mathbf{b}^s\right). \tag{4}$$

The dislocation slip rates are derived using a viscoplastic exponential law (Hutchinson, 1976):

$$\dot{\gamma}^s = \dot{\gamma}_0 \left|\frac{\mathbf{m}^s : \mathbf{S}}{\tau_c^s}\right|^{1/m} sign(\mathbf{m}^s : \mathbf{S}). \tag{5}$$

In Eq. (5), $\dot{\gamma}_0$ is the reference slip rate, m is the strain rate sensitivity exponent, τ_c^s is the critical resolved shear stress on the slip system labeled s, and $\mathbf{S}$ is the deviatoric stress tensor.

2.2. The 1-site VPSC-TGT formulation

For simulating the material response a rate-dependent polycrystalline model is employed. In what follows, we present some features of the 1-site tangent VPSC-TGT formulation. For a more detailed description the reader is referred to Lebensohn and Tomé (1993). This model is based on the viscoplastic behavior of a single crystal and uses a SC homogenization scheme for the transition to the polycrystal. Unlike the FC model, for which the local strain in each grain is considered to be equal to the macroscopic strain applied to the polycrystal, the SC formulation allows each grain to deform differently, according to its directional properties and depending on the strength of the interaction between the grain and its surroundings. In this sense, each grain is in turn considered to be an ellipsoidal inclusion surrounded by a homogeneous effective medium, HEM, which has the average properties of the polycrystal. The interaction between the inclusion and the HEM is solved by means of the Eshelby formalism (Mura, 1987). The HEM properties are not known in advance; rather, they have to be calculated as the average of the individual grain behaviors, once a convergence is achieved. In what follows, we will only present the main equations of the VPSC model.

The deviatoric part of the viscoplastic constitutive behavior of the material at a local level is described by means of the non-linear rate-sensitivity equation:

$$\mathbf{D} = \dot{\gamma}_0 \sum_{s=1}^{\#sys} \mathbf{m}^s \frac{\mathbf{m}^s : \mathbf{S}}{\tau_c^s} \left|\frac{\mathbf{m}^s : \mathbf{S}}{\tau_c^s}\right|^{1/m-1} = \mathbf{M} : \mathbf{S}, \tag{6}$$

where $\mathbf{M}$ is the grain visco-plastic compliance. The interaction equation, which relates the differences between the micro and the macro strain rates $(\mathbf{D}, \bar{\mathbf{D}})$ and deviatoric stresses, $(\mathbf{S}, \bar{\mathbf{S}})$ can be written as follows:

$$\mathbf{D} - \bar{\mathbf{D}} = -\alpha \tilde{\mathbf{M}} : \left(\mathbf{S} - \bar{\mathbf{S}}\right). \tag{7}$$

The interaction tensor $\tilde{\mathbf{M}}$ is given by:

$$\tilde{\mathbf{M}} = \left(\mathbf{I} - \mathbf{S}^{esh}\right)^{-1} : \mathbf{S}^{esh} : \bar{\mathbf{M}}, \tag{8}$$

where $\mathbf{S}^{esh}$ is the Eshelby tensor, $\mathbf{I}$ is the 4th order identity tensor and $\bar{\mathbf{M}}$ is the macroscopic visco-plastic compliance. The parameter α is a scalar that allows tuning the strain compatibility and stress equilibrium constraints. In the present models, the standard TGT approach is used ($\alpha = 1$).

The macroscopic compliance can be adjusted iteratively using the following self-consistent equation:

$$\bar{\mathbf{M}} = \langle \bar{\mathbf{M}} : \mathbf{B} \rangle, \quad \mathbf{B} = \left(\mathbf{M} + \bar{\mathbf{M}}\right)^{-1} : \left(\mathbf{M} + \tilde{\mathbf{M}}\right), \tag{9}$$

where, $\langle \rangle$ denotes a weighted average over all the grains in the polycrystal, and $\mathbf{B}$ is the accommodation tensor defined for each single crystal.

We account for the strain hardening between slip systems by adopting isotropic hardening because we are not focused on the role played by the hardening law. In this case the evolution of the critical shear stresses is given by

$$\dot{\tau}_c = \sum_s h^s |\dot{\gamma}^s|, \tag{10}$$

where h^s are the hardening moduli behaviors, which depend on Γ (accumulated sum of the single-slip contributions to γ^s). These moduli can be written using the initial hardening rate, h_0, and the hardening exponent, n:

$$h^s = h_0 \left(\frac{h_0 \Gamma}{\tau_c^s n} + 1\right)^{n-1}; \quad \Gamma = \sum_s \int_0^t |\dot{\gamma}^s| dt. \tag{11}$$

2.3. MK-VPSC formulation

In their original analysis, Marciniak and Kuczynski postulated the existence of a material imperfection such as a groove or a narrow band across the width of the sheet. In its modified form, proposed by Hutchinson and Neale (1978), an angle Ψ with respect to the x_1 reference direction (Fig. 1) determines the band's orientation. Tensor components are taken with respect to the Cartesian x_i coordinate system, and quantities inside the band are denoted by the subscript b.

The thickness along the minimum section in the band is denoted as $h_b(t)$, with an initial value $h_b(0)$, while an imperfection factor f_0 is given by an initial thickness ratio inside and outside the band:

$$f_0 = \frac{h_b(0)}{h(0)}, \tag{12}$$

with $h(0)$ being the initial sheet thickness outside the groove.

Equilibrium and compatibility conditions must be fulfilled at the interface with the band. Following the formulation developed by Wu et al. (1997), the compatibility condition at the band interface is given in terms of the differences between the velocity gradients $(\bar{\mathbf{L}}, \bar{\mathbf{L}}^b)$ inside and outside the band respectively:

$$\bar{\mathbf{L}}^b = \bar{\mathbf{L}} + \dot{\mathbf{c}} \otimes \mathbf{n} \tag{13}$$

Eq. (13) is decomposed into the symmetric $\bar{\mathbf{D}}$ and screw-symmetric $\bar{\mathbf{W}}$ parts:

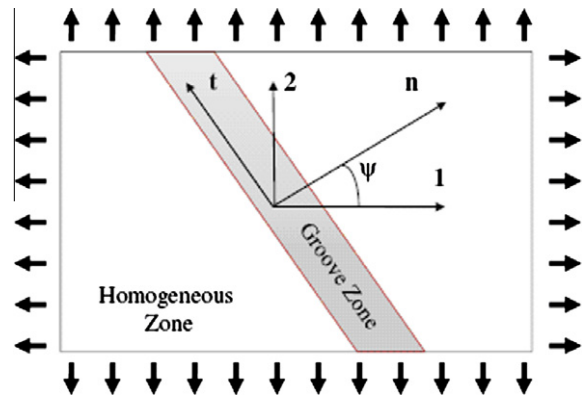**Fig. 1.** Initial defect approach.

$$\bar{\mathbf{D}}^{\mathrm{b}} = \bar{\mathbf{D}} + \frac{1}{2}(\dot{\mathbf{c}} \otimes \mathbf{n} + \mathbf{n} \otimes \dot{\mathbf{c}}), \tag{14}$$

$$\bar{\mathbf{W}}^{\mathrm{b}} = \bar{\mathbf{W}} + \frac{1}{2}(\dot{\mathbf{c}} \otimes \mathbf{n} - \mathbf{n} \otimes \dot{\mathbf{c}}). \tag{15}$$

Here, $\mathbf{n}$ is the unit normal to the band, and $\dot{\mathbf{c}} = [c_1, c_2, 0]$ is a vector to be determined. The equilibrium conditions required at the band interface are given by

$$\mathbf{n}.\bar{\boldsymbol{\sigma}}^{\mathrm{b}} h_{\mathrm{b}} = \mathbf{n}.\bar{\boldsymbol{\sigma}} h, \tag{16}$$

where $\bar{\boldsymbol{\sigma}}$ denotes the Cauchy stress. Noting that δ_{ij} is the Kronecker symbol, the boundary condition $\bar{\sigma}_{33} = 0$ is applied as follows

$$\bar{\sigma}_{\mathrm{ij}} = \bar{S}_{\mathrm{ij}} - \bar{S}_{33}\delta_{\mathrm{ij}} \quad (\mathrm{i} = 1, 2, 3). \tag{17}$$

The integration of the polycrystalline model inside and outside the band is performed in two steps. First, an increment of strain is applied to the material outside the band, $\bar{\mathbf{D}}\Delta t$, while the imposed strain path on the edges of the sheet is assumed to be

$$\rho = \frac{\bar{l}_{22}}{\bar{l}_{11}} = \frac{\bar{d}_{22}}{\bar{d}_{11}} = \mathrm{const}. \tag{18}$$

Keeping the rigid body rotation rate $\bar{\mathbf{w}}$ equal to zero, we assume that $\bar{D}_{13} = \bar{D}_{23} = \bar{w}_{13} = \bar{w}_{23} = 0$ outside and inside the band. The instability appears in a narrow zone inclined an angle Ψ with respect to the major strain axis. The equilibrium and compatibility condition, Eq. (16), can be expressed in the set of axis referenced to the groove – $\mathbf{n}, \mathbf{t}$ – (see Fig. 1). The equilibrium condition implies equality of the force perpendicular to the necking band between both regions:

$$\begin{aligned}\bar{\sigma}^{\mathrm{b}}_{\mathrm{nn}} h_{\mathrm{b}} &= \bar{\sigma}^{h}_{\mathrm{nn}}, \\ \bar{\sigma}^{\mathrm{b}}_{\mathrm{nt}} h_{\mathrm{b}} &= \bar{\sigma}^{h}_{\mathrm{nt}}.\end{aligned} \tag{19}$$

The compatibility condition requires equality of elongation in the longitudinal direction $\mathbf{t}$,

$$\bar{D}^{\mathrm{b}}_{\mathrm{tt}} = \bar{D}_{\mathrm{tt}}. \tag{20}$$

Because, in this research, we are considering thin sheets with the orthotropic axes in the plane of the sheet, in-plane stretching results in a plane-stress state (Kuroda and Tvergaard, 2000). From the plane stress requirement, $\bar{l}^{\mathrm{b}}_{33} = \bar{l}_{33}$ has to be computed in order to satisfy the condition $\bar{\sigma}^{\mathrm{b}}_{33} = \bar{\sigma}_{33} = 0$. In our simulations, the $\bar{l}_{12}$ component is calculated by imposing the requirement that $\bar{\sigma}_{12} = 0$, since we are restricted to orthotropic materials that are loaded along principal axes. The screw component of the velocity gradient within the band is not zero, so the angle of the groove changes as deformation proceeds. The evolution of the groove orientation Ψ is given by

$$\tan(\Psi) = \exp(\varepsilon_{11} - \varepsilon_{22}) \tan(\Psi_0). \tag{21}$$

The system of Eqs. 13, 16 and 17 can be solved to obtain $\dot{\mathbf{c}}$ by substituting the macroscopic analogous Eq. (6) into the incremental form of Eq. (16) and using Eq. (14) to eliminate the strain increments in the band. At any increment of strain along the prescribed strain path, the non-linear system of two equations is solved (Signorelli et al., 2009). In the present simulations, we use Eqs. (19), (20) after obtaining the state $(\bar{\mathbf{L}}, \bar{\boldsymbol{\sigma}})$ in the homogeneous zone, in order to solve the groove state avoiding the 2×2 set of non-linear equations mentioned above. In this case, the remaining unknowns – $\bar{l}^{\mathrm{b}}_{11}, \bar{l}^{\mathrm{b}}_{12}, \bar{l}^{\mathrm{b}}_{33}$ – and – $\bar{\sigma}^{\mathrm{b}}_{22}, \bar{\sigma}^{\mathrm{b}}_{13}, \bar{\sigma}^{\mathrm{b}}_{23}$ – are obtained by solving a mix boundary-condition in the VPSC module, with the logic time benefits.

The analysis is repeated for different values of Ψ_0 (between 0° and 90°). The failure strains $\varepsilon^*_{11}, \varepsilon^*_{22}$ outside the band are obtained after minimization of the curve ε^*_{11} versus Ψ_0. In the present work, the failure condition is reached when $|\bar{D}^{\mathrm{b}}_{33}| > 20|\bar{D}_{33}|$.

Table 1
Material parameters used in the simulations.

Material	FCC-FC	FCC-SC	BCC-FC	BCC-SC
h_0 (GPa)	1.95	2.72	1.85	3.10
n	0.250	0.224	0.250	0.265
τ_c (GPa)	0.0315	0.0470	0.0370	0.0450

3. Numerical results

In this section, we apply the MK-VPSC and MK-FC approaches for predicting FLDs to both FCC and BCC materials. We assumed that plastic deformation occurs by 12 crystallographic slip systems of the type $\{111\}\langle 110 \rangle$ for the FCC material and 48 slip systems of the types $\{110\}\langle 111 \rangle$, $\{112\}\langle 111 \rangle$ and $\{123\}\langle 111 \rangle$ for the BCC. If no single-crystal experiments are available, the crystal level properties are general determined by curve-fitting the stress–strain curve. In previous work (Signorelli et al., 2009), the model evaluations were made by assuming the same properties at the single crystal level. However, in the present case, in order to follow Inal's procedure (Inal et al., 2005), we took the same uniaxial stress–strain curve for all cases: FCC-FC, FCC-SC, BCC-FC and BCC-SC. The material parameters in the constitutive model were estimated by numerically fitting the experimental uniaxial stress–strain response reported by Viatkina et al. (2005) and are listed in Table 1.

An initially random texture, described by 1000 equiaxed grains was assumed, giving the stress–strain responses shown in Fig. 2. In the simulations, the slip resistances τ^s_c of all slip systems are taken equal. For all calculations, the rate sensitivity is $m = 0.02$, and the reference slip rate is $\dot{\gamma}^s_0 = 0.001 \ \mathrm{s}^{-1}$.

The material is assumed to have an imperfection in the form of a groove or band that is initially inclined at an angle ψ with respect to the transverse direction. The initial-thickness ratio inside and outside of the band defines the parameter f_0, which must be fixed. We selected a value of $f_0 = 0.99$ for all the simulations. To analyze the development of deformation localization during proportional straining, the calculations are performed over different strain paths. They are defined in terms of the strain-rate ratios $\rho = \bar{d}_{22}/\bar{d}_{11}$ over the range $-0.5 \leqslant \rho \leqslant 1$ (step = 0.1).

The predicted limit strains are presented in Fig. 3. For each homogenization method, both materials have about the same profile from uniaxial tension ($\rho = -0.5$) to in-plane plane-strain tension ($\rho = 0$). Over this entire range, the major limit strains decrease with increasing ρ. It is important to mention that all simulations were carried out with same imperfection factor;
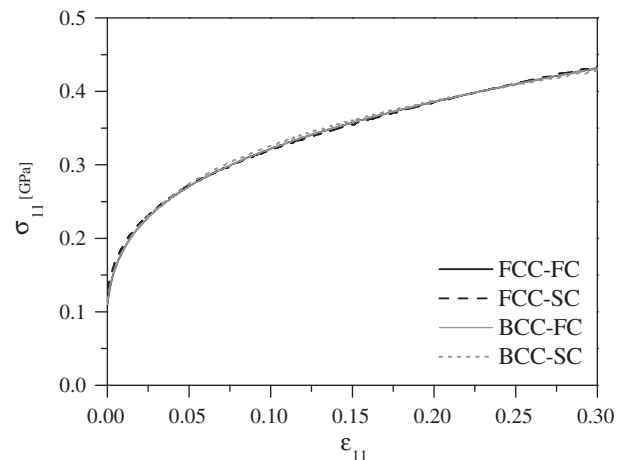

Fig. 2. Tensile stress–strain response for the four materials with FCC and BCC type slip systems and polycrystalline models.
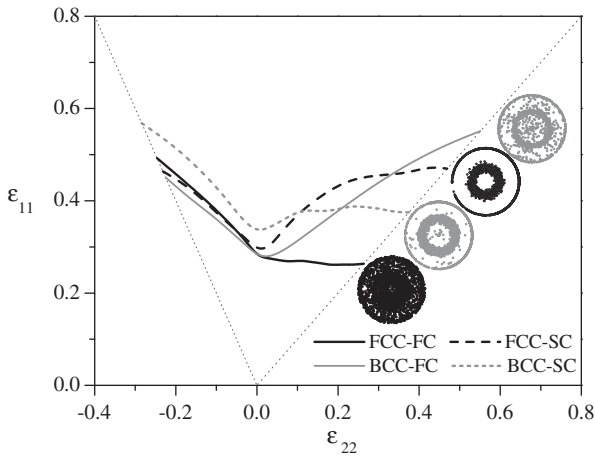
Fig. 3. Influence of the slip microstructure and interaction model on the FLD.

Fig. 4. Stress potential at equi-biaxial failure for all tested materials.

consequently, the predicted FLD_0 is not the same for all the cases. However, it can be seen that, for the BCC-SC material, the largest value of the parameter n results in the highest limit values. This in agreement with the conventional wisdom that as n increases so do the limit strains. Details of this behavior can be found in Serenelli et al., 2010 for the case of a BCC material assuming either 24 or 48 slip systems. Also, it is interesting to note that MK-FC simulations using same n value predict similar limit strains for the in-plane plane strain condition.

Predictions begin to diverge in the biaxial-stretching range. Here, results clearly illustrate large differences between the homogenization schemes and between materials. These differences reach a maximum for the equi-biaxial deformation path. The MK-FC framework predicts both the highest and lowest limit strains, for the BCC and FCC materials respectively. The MK-FC FCC material calculation leads to a remarkably low limit curve. Completely the opposite behavior is observed within the MK-VPSC scheme. In this case, the FCC material shows better formability than the BCC for $\rho \geqslant 0.3$, and for both materials, the calculated limit-strain curves remain between those calculated with the MK-FC scheme near the equi-biaxial zone. In the case of the FCC material, MK-VPSC approach predicts a noticeable increase of the limit strains over the whole right side of the diagram, while the BCC material only shows that behavior in the region $0 \leqslant \rho \leqslant 0.6$. For $\rho \geqslant 0.6$, the MK-VPSC limit-strain values are nearly constant. It is interesting to note that our results for the MK-FC's calculations are very close to those reported by Inal et al. (2005) for the FCC material. However, our BCC-FC's values are lower than Inal's, which we attributed to the fact that in our simulations we assume 48 slip systems (Serenelli et al., 2010).

It should be to be noted that we determined the values of the material constants in order to reproduce the same stress–strain curve. To highlight the fact that differences in the FLD profiles are attributed to the homogenization scheme, we repeated the calculations shown in Fig. 3 but assumed that all the material parameters at the single crystal level are the same for the tested models. Simulation results are given in Appendix I.

Fig. 3 also includes the {100} stereographic pole figures of each material at the end of the equi-biaxial stretching path. As can be seen, FCC and BCC material textures evolve differently depending on the model assumption. For FCC, the FC model develops a weaker texture than that produced by the VPSC calculation. For the BCC case, the final textures are qualitatively similar but quantitatively different in their degree of intensity.

According to Lian et al. (1989), the yield-surface shape has a tremendous effect on the FLD, and Neale and Chater (1980) demon-
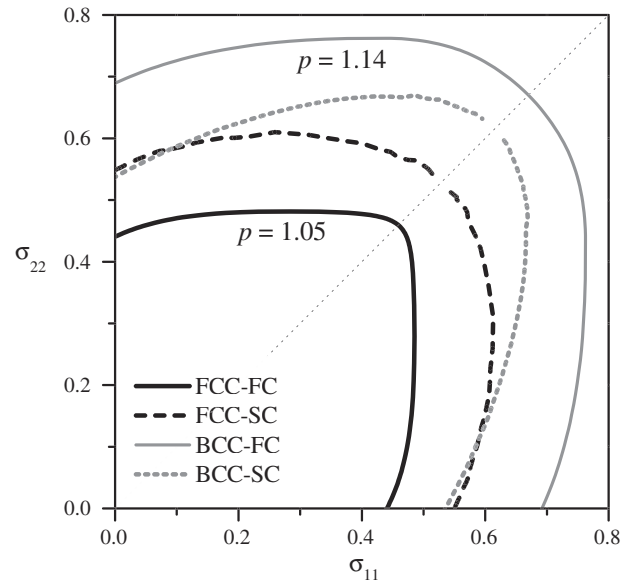
strated that a decrease in the sharpness of the stress potentials in equi-biaxial stretching promotes larger limit strains. A sharp curvature allows the material to quickly select a deformation path approaching plane strain, and this results in the prediction of a relatively low limit strain. The yield potentials of the materials were calculated by imposing different plastic strain-rate tensors under a state of plane stress in $\sigma_{11} - \sigma_{22}$ space. With the simulation, we deformed the material in equi-biaxial stretching up to a given plastic strain and then performed the yield-locus calculations. For the purpose of comparing polycrystal yield surfaces, all work-rates were normalized to that of FCC-FC uniaxial stretching. We calculated the yield loci corresponding to each of the necking limit strains, in order to highlight the link between the yield-surface shape and the forming-limit behavior. Shapes and curvatures predicted by the FC and VPSC models are shown in Fig. 4.

As expected, the curvature of the yield locus of the FCC-FC material in the equi-biaxial stretching zone is much sharper than those of the other materials, which is consistent with its lowest limit-strain value shown in Fig. 3. Similarly, the curvature of the BCC-FC yield locus is rounder than the others, again in agreement with the predicted limit strains. We also calculated Barlat's parameter p[1] (Barlat et al., 1989) for our materials – Barlat proposed the parameter p to quantify the effect of yield-surface shape on limit-strains – finding that the values of p for the FCC-FC and BCC-FC materials are the lowest and the highest, respectively (see Fig. 4).

The influence of texture evolution has been previously discussed by several authors. Tóth et al. (1996) performed simulations with a rate-independent Taylor model, showing that crystal rotations decrease the limit strains. Wu et al. (2004b) used a mesoscopic approach and an FC scheme to demonstrate that texture evolution increases the limit strains in the biaxial zone. Inal et al. (2005) showed that texture development does not have a significant influence on the FLD. In our opinion, the opposite trends in forming-limit values found by previous researchers cannot be justified based only on initial textures. We believe that these differences are related to material anisotropy and its evolution along the deformation path. This evolution produces an increase or decrease of the FLD profile. To determine the effect of texture evolution on

---

[1] p is the ratio between the yield stress in plane-strain σ_p to that in equi-biaxial tension σ_b.
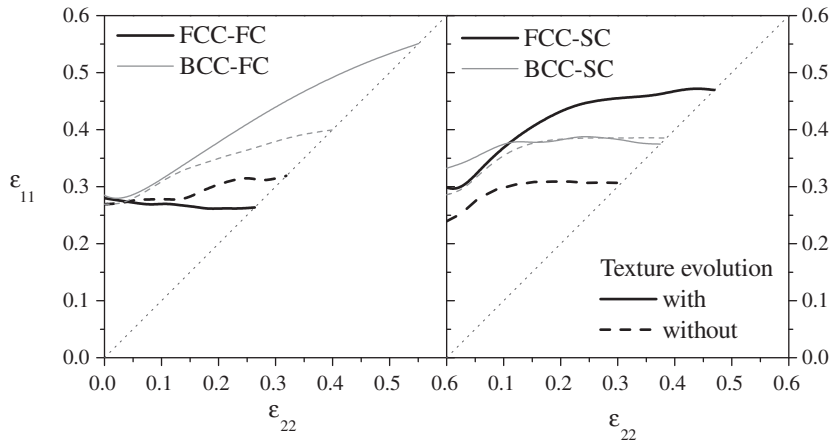
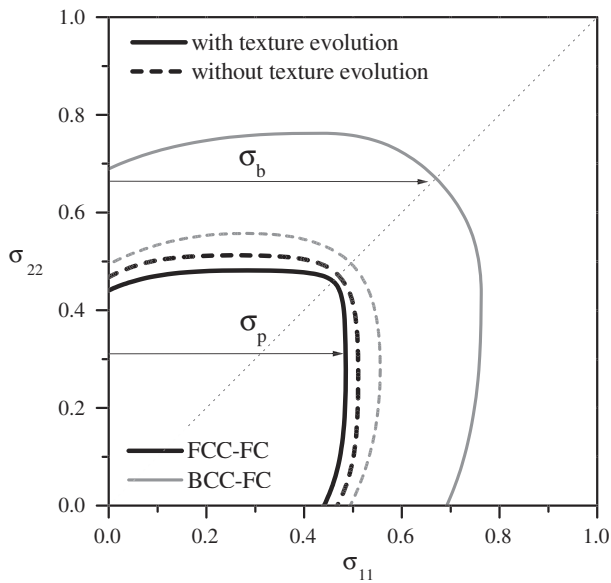**Fig. 5.** Influence of the texture evolution on the limit strains.

Fig. 6. Stress potential at equi-biaxial failure.

Table 2
p parameter for the FCC-FC and BCC-FC equi-biaxial stretching cases.

Material	Texture evolution	P
FCC-FC	Yes	1.050
BCC-FC	Yes	1.139
FCC-FC	No	1.090
BCC-FC	No	1.120

anced-biaxial tension, except for the BCC-SC case. Within the VPSC framework, BCC simulations carried out with and without texture evolution have practically identical shapes, except in the region $0 \leqslant \rho \leqslant 0.3$, where minor differences are observed. However, results for the FCC-SC material are quite different in the biaxial zone, and are consistent with those shown in a previous work (Signorelli et al., 2009). In this case, anisotropy evolution, through textural changes, produces greater limit strains.

On the other hand, the MK-FC formulation predicts different limit-strain profiles with and without texture updating. For each material, the limit-strain values are very close for strain ratios $\rho \leqslant 0.4$, but the predictions begin to diverge for $\rho \geqslant 0.5$, and the differences increase continuously until reaching a maximum for equi-biaxial deformation. While texture evolution produces better formability for the BCC case, the tendency is the opposite for FCC, which has higher limit values without texture updating. To better understand these results, we calculated the FC stress-potentials (Fig. 6). When the initial texture is updated, the FCC yield potential

the limit strains, we repeated the calculations shown in Fig. 3 but with the random texture fixed in its initial state (Fig. 5). Our results show that texture evolution is important, particularly near bal-
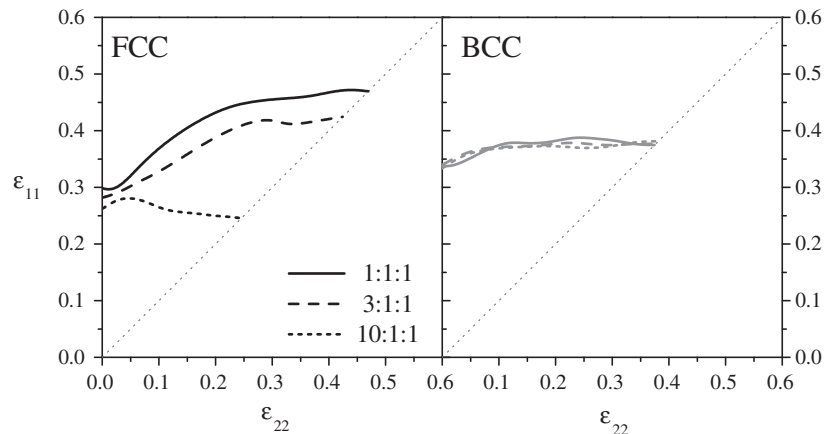

Fig. 7a. Influence of the initial grain shape on the limit strains.

is sharper and the BCC's is blunter. It can be seen that, for the BCC material, the sharpness of the yield potential in equi-biaxial stretching decreases with texture evolution. The opposite behavior is observed for the FCC case.

The calculated p parameters for the cases displayed in Fig. 6 are shown in Table 2. It should be noted that the trends followed by this parameter and the limit-strain values are consistent. Concerning the MK-VPSC simulations, the effect of texture development is not so visible when yield loci are analyzed, though a strong influence on the forming limits is observed for the FCC material.

Formability may also be influenced by other microstructural parameters, such as the grain shape. As the VPSC model has the capability to take into account the grain shape and its evolution, we studied the influence of the average grain-shape's aspect ratio on the FLDs. The numerical simulations corresponding to three different aspect ratios are presented in Fig. 7a. For the FCC material (left), differences are observed, especially when the aspect ratio is more pronounced. For initially aspect ratios of (1:1:1) and (3:1:1), the profiles show no significant changes. But for an elongated grain with an aspect ratio of (10:1:1), a noticeable decrease of the limit-strain values is observed.

To gain insight into this behavior, we present the textures calculated at the end of the equi-biaxial loading path in Fig. 7b. For both material structures, and for the different aspect-ratio grains, we relate the simulated FLDs to the predicted final textures at failure. The BCC final textures, which are qualitatively and quantitatively very similar, are consistent with the minor changes observed in the BCC limit profiles. Though the microscopic shape of grains is quite different, the texture seems largely unaffected. One reason which may explain this behavior is the additional slip planes in the BCC material, triggering an increase in freedom for the selection of the active slip systems. We believe that the basic qualitative features of the simulated texture evolution of initially random-textured materials is only weakly related to the microstructure within each single grain, and the main influence has to be attributed to the available slip systems. This point is made to show that deviations from compatibility do not always have an effect on texture development. Furthermore, it is important to highlight that the predicted stress–strain response shows negligible differences over the entire biaxial stretching range. To the contrary, for the FCC case, grain-shape effects matter and there is a notable difference in the predicted final textures at failure, especially for the case of very elongated grains. For the elongated-grain, FCC materials, the differences diminish as deformation approaches

plane strain. There, very similar limit values correspond to nearly equal final textures.

The above results should not be regarded as a simulation of a specific material, but rather an assessment of the consequences of FCC and BCC crystallographic slip assumptions in conjunction with the transition scale model applied to FLDs. The validity of a numerical simulation is demonstrated in its ability to accurately reproduce experimental data. We know that many factors influence forming-limit predictions through the M–K approach, the homogenization scheme being one of the most important. In the next section, comparisons to experimental data are used to test and validate the MK-VPSC model.

4. Comparison to experimental FLDs

Here, the predicted limit-strain values are compared to experimental data for an aluminum-alloy and a DQ-type steel. For the AA5182-O alloy, we combined the experimental data – FLD and strain–stress curve – from Wu et al. (2003) with the reference plastic shearing rate and shear strain-rate sensitivity from the previous section. The initial texture of the material was measured using a Phillips X'Pert X-ray diffractometer, and discretized into 1000 orientations with an equal volume fraction weighting to generate the ODF (orientation distribution function). The {111} and {200} stereographic pole figures are shown in Fig. 8. As can be seen, this material had a weak preferred orientation. At this point, we want
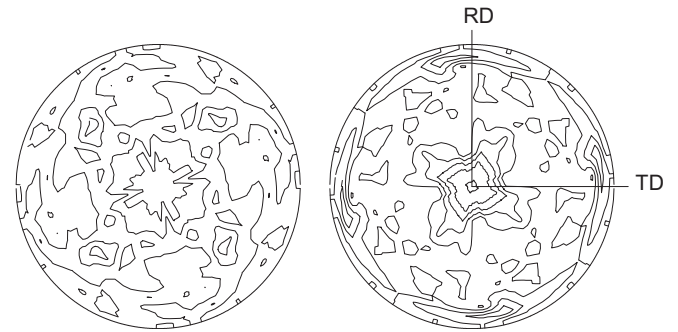

Fig. 8. Initial measured AA5182-O texture represented by {111} and {200} stereographic pole figures, left and right respectively. Lines are multiples of a half-random distribution (m.r.d.).
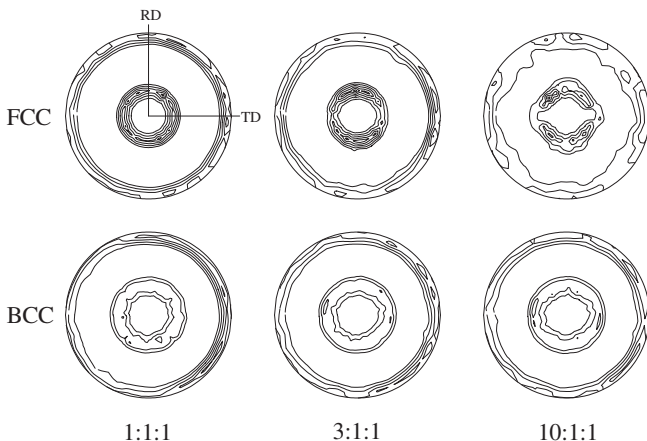

Fig. 7b. Stereographic {111} (top) and {110} (bottom) pole figures showing the final textures in equi-biaxial failure. Lines are multiples of a random distribution (m.r.d.).
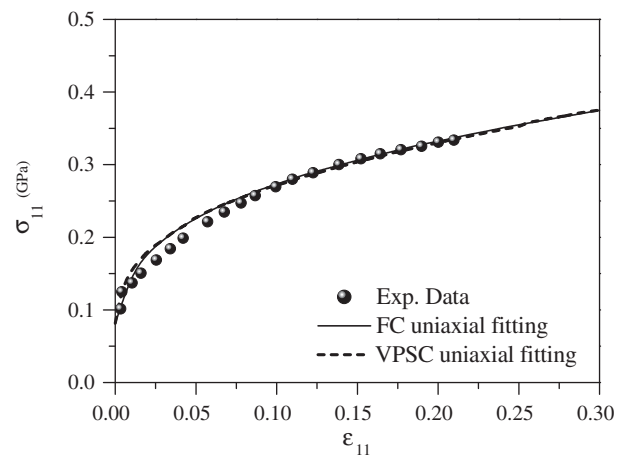

Fig. 9. Tensile stress–strain responses in uniaxial tension for the AA5182-O alloy. The fitting parameters were: (FC) $m = 0.02$, $\tau_c = 24$ MPa, $h_0 = 2500$ MPa, $n = 0.260$; (VPSC) $m = 0.02$, $\tau_c = 30$ MPa, $h_0 = 4000$ MPa, $n = 0.245$.
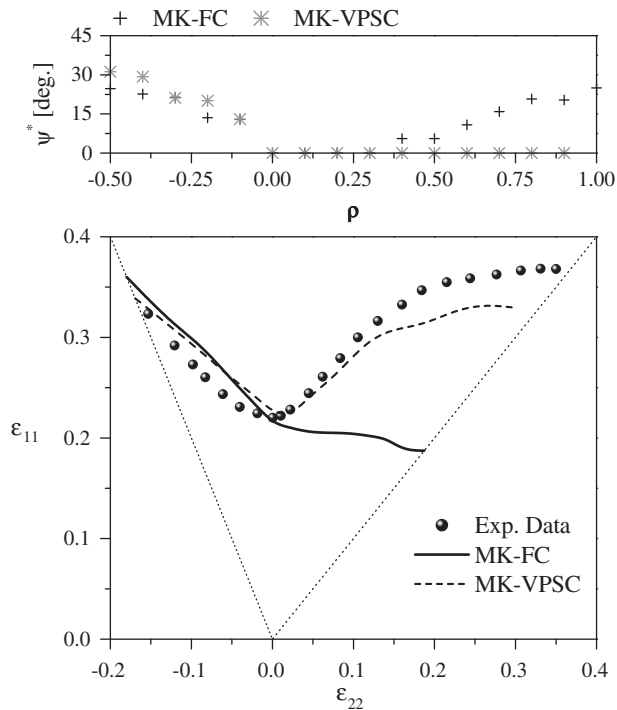
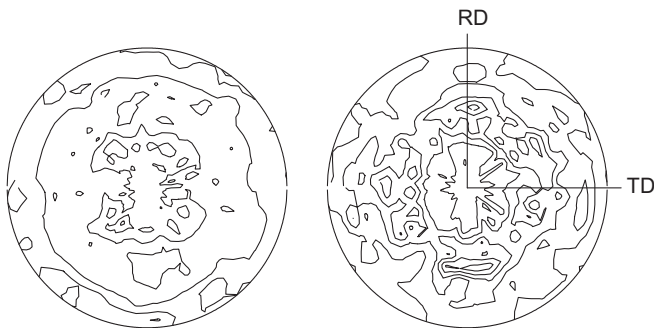**Fig. 10.** Experimental and calculated FLDs for the AA5182-O alloy.

Fig. 11. Experimental {110} and {100} stereographic pole figures, left and right respectively. Lines are multiples of a half-random distribution (m.r.d.).

to underscore that this weak texture should be adequate for validating our results. For the purpose of the simulations, equiaxed grains were assumed. The material hardening parameters used in the VPSC model were estimated by numerically fitting the experimental uniaxial stress–strain response and accounting for the

strain hardening between slip systems. By adopting isotropic hardening, an initial critically resolved shear stress $\tau_c = 30$ MPa, a hardening rate $h_0 = 4000$ MPa and an exponent $n = 0.245$ were found. In the case of the full constraint model, we assumed values of $\tau_c = 24$ MPa, $h_0 = 2500$ MPa and $n = 0.260$. The correspondence between the calculated responses and the experimental strain–stress curve is shown in Fig. 9.

For calculating the FLD the value of the initial imperfection parameter, f_0, cannot be easily correlated with experimental measurements. In our calculations we have chosen the value of f_0 to match the experimental plane-strain limit value. Imperfection factors of $f_0 = 0.960$ and $f_0 = 0.965$ were required for MK-VPSC and MK-FC approaches, respectively.

The FLD predictions for this alloy are compared to the experimental data in Fig. 10. The predicted trend of the MK-VPSC's limit-values agrees well with experimental data over the whole range of ρ, though our simulations tend to underestimate the limit strains as ρ approaches equi-biaxial stretching. A better prediction of the limit values near equi-biaxial stretching could have been obtained if smaller initial imperfection values had been assumed. However, even the current simulation overestimates the uniaxial data. A smaller initial imperfection would accentuate this discrepancy. The calculated FLD using the FC approach is also plotted. This curve only agrees well with the experimental data for $\rho \leqslant 0$. In the biaxial zone, the model severely under predicts the experimentally observed limit strains. The lack of agreement along the biaxial path found using the MK-FC approach can be fully remedied using MK-VPSC model. At the top of Fig. 10, we show the orientation (angle) of the geometrical defect at failure, which minimizes the forming limit strains and their dependency on the strain path for both models. A clear difference is observed for biaxial loading paths. In the case of AA5182-O alloy, using MK-FC, the initial orientation that corresponds to the critical strains increase from 0 to 25 degrees for $\rho = 0.4$ to $\rho = 1.0$. While for MK-VPSC the initial band orientation is always zero over the whole right-hand side of the FLD. Moreover, minimal differences are calculated for band orientations from 0 to 45 degrees. In the next example, we will show that this behavior is completely different when an initially textured material is considered.

It is generally accepted that most of the aluminum alloys experience a saturation of their hardening behavior. Thus, we fitted the saturation law presented in Signorelli et al. (2009) for the same aluminum alloy, in addition to the Swift formulation, and calculated the resulting FLDs. These results are not shown in Fig. 10 since the profiles and limit-values for both hardening models are quite similar. Even though the MK-VPSC model compares well with the AA5182-O FLD data, other important factors could be taken into account to improve the simulations, particularly near equi-biaxial stretching. Such factors might include a dislocation-strain work-hardening based model, to complement the crystallographic texture information.
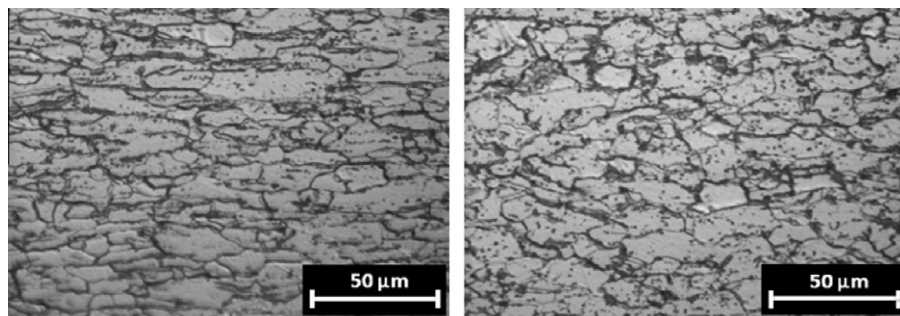

Fig. 12. Longitudinal (left) and transversal (right) optical micrographs for the DQ-type steel.
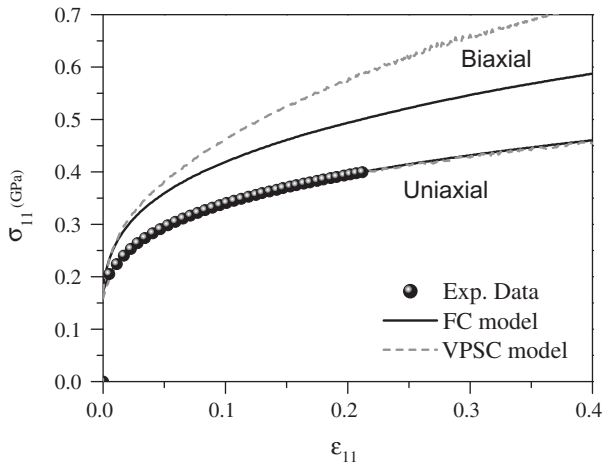
Fig. 13. Tensile stress–strain responses in uniaxial tension for the DQ type steel. The fitting parameters are: (FC) $m = 0.02$, $\tau_c = 55$ MPa, $h_0 = 1100$ MPa, $n = 0.209$; (VPSC) $m = 0.02$, $\tau_c = 62$ MPa, $h_0 = 2275$ MPa, $n = 0.222$.

To extend our MK-FC and MK-VPSC simulations to the case of a BCC structure, we investigated an electro-galvanized, DQ-type steel, sheet 0.67 mm thick. All experimental tests were conducted at room temperature. Using X-ray diffraction, the initial incomplete poles figures for the {110}, {200} and {112} diffraction peaks were measured, and from these data, we calculated the ODF and the complete {110} and {100} poles figures. These pole figures are shown in Fig. 11.

Optical micrographs (Fig. 12) show a typical ferrite–perlite microstructure with grains slightly elongated in the rolling direction. For the purpose of the simulations, we assumed all grains had an approximately aspect ratio of (1.5:1.0:1.0).

Following the ASTM E8M norm, tensile tests were performed on specimens cut along the rolling direction. In the case of DQ-type, and most other steel sheets, the use of Swift's hardening law rather than the Voce law is generally accepted. In order to obtain virtually identical uniaxial tensile responses, we calculated two sets of hardening parameters for the constitutive model by curve fitting from numerical simulations: $\tau_c = 62$ MPa, $h_0 = 2275$ MPa, $n0.222$ for the VPSC model and $\tau_c = 55$ MPa, $h_0 = 1100$ MPa, $n = 0.209$ for the FC case. Fig. 13 compares experimental and simulated stress–strain curves, for both models, under uniaxial tension. The experimental and the two simulated curves are superimposed. However, the predicted limit strain at necking generated through a M–K model, is different for the FC and VPSC simulations. An extension of the calculated strain–stress values up to $\varepsilon = 0.40$, was plotted in order to illustrate the large-strain behaviors. Also, the FC and VPSC predictions of biaxial hardening are shown for reference.

The forming limit diagram was determined by following Hecker's technique (Charca Ramos et al., 2010). The standard experimental procedure involved three stages: applying a circle grid to the samples, punch stretching to maximum load, and measurement of strains. A grid pattern of 2.50 mm diameter circles was printed on sheet samples by electrochemical grid-marking technique. For stretching, the gridded side of the specimen was located opposite the punch. We were able to obtain strain states between and including biaxial and uniaxial tension by varying sample widths and lubrication conditions. A 100 kN capacity single action hydraulic press (INSTRON 3382 machine) loaded the Nakajima hourglass geometry specimens with a 40 mm diameter hemispherical punch. Major and minor deformed circle diameters, measured
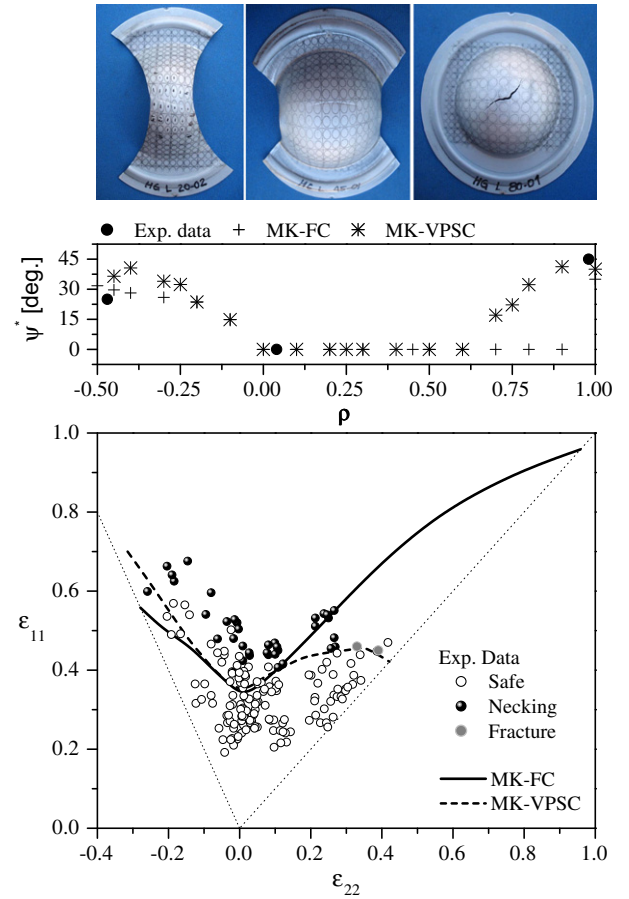

Fig. 14. (Top) Photographs of the gridded specimens after approximate uniaxia (left), plane-strain tension (center) and equi-biaxial stretching (right) tests.

with a profile projector, gave the major and minor true strains, ε_1 and ε_2, lying in safe, necked and fractured regions. A more detailed description of the experimental procedure can be found in Charca Ramos et al. (2010).

Before performing simulations, we adjusted f_0 such that the predicted limit strains matched the experimental results in plane strain. For the MK-FC and MK-VPSC simulations these values of f_0 were 0.999 and 0.996 respectively. Together with the experimental data, the simulated FLDs for both the MK-FC and MK-VPSC schemes are shown in Fig. 14. In the biaxial quadrant of strain space, we found that the limit values predicted by MK-VPSC accurately separate the regions of safe (uniform) and insecure (localized) deformation. To the contrary, the critical values calculated with the MK-FC approach, are only accurate for strain path values to 0.3. Our simulations clearly show that limit values calculated with the MK-FC approach increase unrealistically as ρ increases. It is clear that the VPSC scheme together with the M–K approach provides accurate predictions of the DQ-type steel behavior over the entire biaxial range. On the tensile side of plane strain, the MK-FC model predicts lower values than MK-VPSC, though both approaches appear to be accurate. The predicted critical orientation of the geometrical defect, which minimizes the limit strains for both models, is in good agreement with the experimental data. Nevertheless, some differences in the profiles for both models arise in the biaxial zone.

(Bottom) Experimental and calculated FLDs for the DQ-type steel.

5. Conclusions

In this paper, we calculated forming-limit strains using both full-constraint and self-consistent rate-dependent, polycrystal-plasticity models together with the Marciniak–Kuczynski approach. We focused on the consequences of the FCC and BCC crystallographic-slip assumptions, coupled with the selection of either FC or SC type grain-interactions.

Non-textured FCC and BCC materials were investigated, imposing same uniaxial behaviors for all simulations. The FLD results clearly depended on the homogenization scheme, and we explained the differences in terms of the sharpness of the yield-loci and texture development. The MK-FC framework predicts both the highest and lowest limit strains, for the BCC and FCC materials respectively. Within this framework, our results are the same as Inal's. However, by using the MK-VPSC approach, we predict more reliable values. The influence of the texture evolution was also analyzed. Our simulations show that texture evolution is important, particularly near balanced-biaxial tension, except for the BCC-SC case.

To verify the capability of the MK-VPSC model to predict actual experimental limit strains, observed for either FCC or BCC structures, we carried out simulations for an aluminum alloy and DQ-type steel. For the AA5182-O alloy, the predicted trend of the MK-VPSC's limit-values agrees well with experimental data over the whole strain-path range, though our simulations tend to underestimate the limit strains as we approaches to equi-biaxial stretching. The DQ-type steel simulations provide good prediction of the steel's behavior over the complete biaxial range. On the tensile side of plane strain, MK-FC predicts lower values than MK-VPSC, though both approaches appear to be accurate. Taking into account these FLD predictions, we can conclude that the better description of the material behavior given by the self-consistent scheme leads to more realistic forming-limit predictions.

Additions to the present approach could be made in order to improve the forming-limit predictions. For example, the adaptation of the VPSC model with the Affine self-consistent model would be of great interest, as Wang et al. (2010) pointed out in their research. In addition, the inclusion of a dislocation-strain work-hardening based models could be helpful, particularly for predicting macroscopic behavior under strain-path changes. These improvements are in progress and will be reported elsewhere.

Acknowledgements

Appendix A

To highlight the fact that differences in the macroscopic response are attributed to the homogenization scheme, we repeated the calculations shown in Fig. 3 but assumed that all the material parameters at the single crystal level were the same for the tested models. In the following figures we compare the results. It is clear that the MK-VPSC FLD predictions are qualitative the same whether calculated from the set of parameters obtained by independently curve-fitting the tension curve or by using the same set of parameters employed in the MK-FC simulations. The top figure shows the simulations corresponding to a FCC type material and the bottom to a BCC crystal structure (see Fig. A1).
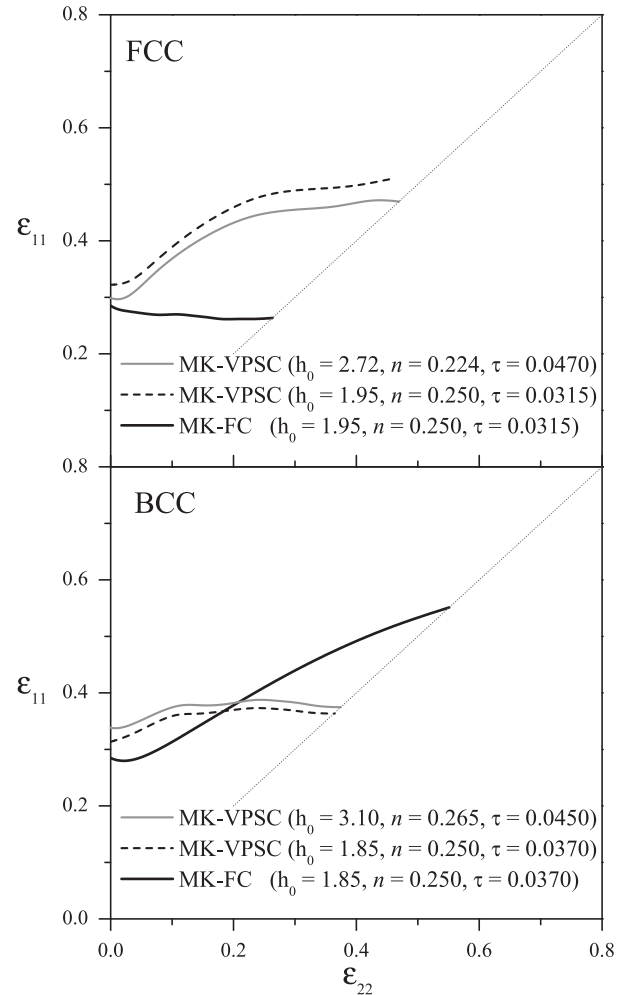

Fig. A1. Influence of the material parameters at single crystal level for both homogenization approaches on the FLD: FCC (top) and BCC (bottom).

References

Ávila, A., Vieira, E., 2003. Proposing a better forming limit diagram prediction: a comparative study. J. Mater. Process. Technol. 141, 101–108.

Banabic, D., Dannenmann, E., 2001. Prediction of the influence of yield locus on the limit strains in sheet metals. J. Mater. Process. Technol. 109, 9–12.

Banabic, D., Comsa, S., Jurco, P., Cosovici, G., Paraianu, L., Julean, D., 2004. FLD theoretical model using a new anisotropic yield criterion. J. Mater. Process. Technol. 157–158, 23–27.

Barlat, F., 1987. Crystallographic texture, anisotropic yield surface and forming limits of sheet metals. Mat. Sci. Eng. 91, 55–72.

Barlat, F., 1989. In: Forming limit diagrams-predictions based on some microstructural aspects of materials. In: Wagoner, R.H., Chan, K.S., Keeler, S.P. (Eds.), . Forming Limit Diagrams: Concepts, Methods and Applications. The Minerals, Metals and Materials Society, Warrendale, PA, pp. 275–302.

Butuc, M.C., Banabic, D., Barata da Rocha, A., Gracio, J.J., Ferreira Duarte, J., Jurco, P., Comsa, D.S., 2002. The performance of Yld96 and BBC2000 yield functions in forming limit prediction. J. Mater. Process. Technol. 125–126, 281–286.

Butuc, M.C., Barata da Rocha, A., Gracio, J.J., Ferreira Duarte, J., 2003. Study on forming limit diagrams prediction using a phenomenological and a physical approach of plasticity theory. J. Phys. IV (France) 105, 73–80.

Butuc, M.C., 2004. Forming Limit Diagrams. Definition of Plastic Instability Criteria. Ph.D. Thesis, Engineering Faculty of Porto University.

Cao, J., Yao, H., Karafillis, A., Boyce, M.C., 2000. Prediction of localized thinning in sheet metal using a general anisotropic yield criterion. Int. J. Plast. 16, 1105–1129.

Charca Ramos, G., Stout, M., Bolmaro, R.E., Signorelli, J.W., Serenelli, M., Bertinetti, M.A., Turner, P., 2010. Study of a drawing-quality sheet steel. II: Forming-limit curves by experiments and micromechanical simulations. Int. J. Solids Struct. 47, 2294–2299.

Dreyer, C.E., Chiu, W.V., Wagoner, R.H., Agnew, S.R., 2010. Formability of a more randomly textured magnesium alloy sheet: application of an improved warm sheet formability test. J. Mater. Proc. Tech. 210, 37–47.

Hill, R., 1993. A user-friendly theory of orthotropic plasticity in sheet metals. Int. J. Mech. Sci. 35, 19–25.

Hiwatashi, S., Van Bael, A., Van Houtte, P., Teodosiu, C., 1998. Predictions of forming limit strains under strain-path changes: application of an anisotropic model based on texture and dislocation structure. Int. J. Plast. 14, 647–669.

Hutchinson, J.W., 1976. Bound and self-consistent estimated for creep of polycrystalline materials. Proc. R. Soc. Lond. A348, 101–127.

Hutchinson, J.W., Neale, K.W., 1978. Sheet necking II, time-independent behavior. In: Koistinen, D.P., Wang, N.M. (Eds.), Mechanics of Sheet Metal Forming. Plenum Press, New York-London, pp. 127–153.

Inal, K., Neale, K., Aboutajeddine, A., 2005. Forming limit comparison for FCC and BCC sheets. Int. J. Plast. 21, 1255–1266.

Keeler, S.P., Backofen, W.A., 1964. Plastic instability and fracture in sheet stretched over rigid punches. ASM Trans. Quart. 56, 25–48.

Knockaert, R., Chastel, Y., Massoni, E., 2002. Forming limits predictions using rate-independent polycrystalline plasticity. Int. J. Plast. 18, 231–247.

Kuroda, M., Tvergaard, V., 2000. Forming limit diagrams for anisotropic metal sheets with different yield criteria. Int. J. Solids Struct. 37, 5037–5059.

Lebensohn, R.A., Tomé, C.N., 1993. A self-consistent approach for the simulation of plastic deformation and texture development of polycrystals: application to zirconium alloys. Acta Metall. Mater. 41, 2611–2624.

Lian, J., Barlat, F., Baudelet, B., 1989. Plastic behavior and stretchability of sheet metals. II. Effect of yield surface shape on sheet forming limit. Int. J. Plast. 5, 131–147.

Marciniak, Z., Kuczynski, K., 1967. Limit strains in the processes of stretch-forming sheet metal. Int. J. Mech. Sci. 9, 609–620.

Mura, T., 1987. Micromechanics of Defects in Solids. Martinus Nijhoff Publishers, Dordrecht, The Netherlands.

Neale, K.W., Chater, E., 1980. Limit strain predictions for strain-rate sensitive anisotropic sheets. Int. J. Mech. Sci. 22, 563–574.

Neil, C.J., Agnew, S.R., 2009. Crystal plasticity-based forming limit prediction for non-cubic metals: application to Mg alloy AZ31B. Int. J. Plast. 25, 379–398.

Serenelli, M.J., Bertinetti, M.A., Signorelli, J.W., 2010. Investigation of the dislocation slip assumption on formability of BCC sheet metals. Int. J. Mech. Sci. 52, 1723–1734.

Signorelli, J.W., Bertinetti, M.A., 2009. On the role of constitutive model in the forming limit of FCC sheet metal with cube orientations. Int. J. Mech. Sci. 51, 473–480.

Signorelli, J.W., Bertinetti, M.A., Turner, P.A., 2009. Predictions of forming limit diagrams using a rate-dependent polycrystal self-consistent plasticity model. Int. J. Plast. 25, 1–25.

Tóth, L., Hirsch, J., Van Houtte, P., 1996. On the role of texture development in the forming limits of sheet metals. Int. J. Mech. Sci. 38, 1117–1126.

Viatkina, E.M., Brekelmans, W.A., Geers, M., 2005. A crystal plasticity based estimate for forming limit diagrams from textural inhomogeneities. J. Mater. Proc. Tech. 168, 211–218.

Wang, H., Raeisinia, B., Wu, P.D., Agnew, S.R., Tomé, C.N., 2010. Evaluation of self-consistent polycrystal plasticity models for magnesium alloy AZ31B sheet. Int. J. Solids Struct. 47, 2905–2917.

Wu, P.D., Neale, K.W., Van der Giessen, E., 1997. On crystal plasticity FLD analysis. Proc. R. Soc. Lond. A 453, 1831–1848.

Wu, P.D., Neale, K.W., Van der Giessen, E., Jain, M., Makinde, A., MacEwen, S.R., 1998. Crystal plasticity forming limit diagram analysis of rolled aluminum sheets. Metal. Mater. Trans. 29A, 527–535.

Wu, P.D., Jain, M., Savoie, J., MacEwen, S.R., Tugcu, P., Neale, K.W., 2003. Evaluation of anisotropic yield functions for aluminum sheets. Int. J. Plast. 19, 121–138.

Wu, P.D., MacEwen, S.R., Lloyd, D.J., Neale, K.W., 2004a. Effect of cube texture on sheet metal formability. Mater. Sci. Eng. A 364, 182–187.

Wu, P.D., MacEwen, S.R., Lloyd, D.J., Neale, K.W., 2004b. A mesoscopic approach for predicting sheet metal formability. Model. Simul. Mater. Sci. Eng. 12, 511–527.

Wu, P.D., Graf, A., Mac Ewen, S.R., Lloyd, D.J., Jain, M., Neale, K.W., 2005. On forming limit stress diagram analysis. Int. J. Solids Struct. 42, 2225–2241.

Wu, P.D., Lloyd Jain, D.J.M., Neale, K.W., 2007. Effects of spatial grain orientation distribution and initial surface topography on sheet metal necking. Int. J. Plast. 23, 1084–1104.

Yoshida, K., Ishizaka, T., Kuroda, M., Ikawa, S., 2007. The effects of texture on formability of aluminum alloy sheets. Acta Mater. 55, 4499–4506.

Zhou, Y., Neale, K.W., 1995. Predictions of forming limit diagrams using a rate-sensitive crystal plasticity model. Int. J. Mech. Sci. 37, 1–20.